

## DETECTION OF ANOMALOUS MICROWAVE EMISSION IN THE PLEIADES REFLECTION NEBULA WITH *WILKINSON MICROWAVE ANISOTROPY PROBE* AND THE COSMOSOMAS EXPERIMENT

R. GÉNOVA-SANTOS<sup>1,2</sup>, R. REBOLO<sup>1,2,3</sup>, J. A. RUBIÑO-MARTÍN<sup>1,2</sup>, C. H. LÓPEZ-CARABALLO<sup>1,2</sup>, AND S. R. HILDEBRANDT<sup>1,4</sup>

<sup>1</sup> Instituto de Astrofísica de Canarias, C/Vía Láctea s/n, E-38200 La Laguna, Tenerife, Spain

<sup>2</sup> Departamento de Astrofísica, Universidad de La Laguna (ULL), E-38206 La Laguna, Tenerife, Spain

<sup>3</sup> Consejo Superior de Investigaciones Científicas, Spain

<sup>4</sup> California Institute of Technology, 1200 East California Boulevard, Pasadena, CA 91125, USA

Received 2011 June 13; accepted 2011 September 12; published 2011 November 22

### ABSTRACT

We present evidence for anomalous microwave emission (AME) in the Pleiades reflection nebula, using data from the seven-year release of the *Wilkinson Microwave Anisotropy Probe* and from the COSMOSOMAS (Cosmological Structures on Medium Angular Scales) experiment. The flux integrated in a  $1^\circ$  radius around R.A. =  $56^\circ 24'$ , decl. =  $23^\circ 78'$  (J2000) is  $2.15 \pm 0.12$  Jy at 22.8 GHz, where AME is dominant. COSMOSOMAS data show no significant emission, but allow one to set upper limits of 0.94 and 1.58 Jy (99.7% confidence level), respectively, at 10.9 and 14.7 GHz, which are crucial to pin down the AME spectrum at these frequencies, and to discard any other emission mechanisms which could have an important contribution to the signal detected at 22.8 GHz. We estimate the expected level of free–free emission from an extinction-corrected  $H\alpha$  template, while the thermal dust emission is characterized from infrared DIRBE data and extrapolated to microwave frequencies. When we deduct the contribution from these two components at 22.8 GHz, the residual flux, associated with AME, is  $2.12 \pm 0.12$  Jy ( $17.7\sigma$ ). The spectral energy distribution from 10 to 60 GHz can be accurately fitted with a model of electric dipole emission from small spinning dust grains distributed in two separated phases of molecular and atomic gas, respectively. The dust emissivity, calculated by correlating the 22.8 GHz data with  $100 \mu\text{m}$  data, is found to be  $4.36 \pm 0.17 \mu\text{K} (\text{MJy sr}^{-1})^{-1}$ , a value considerably lower than in typical AME clouds, which present emissivities of  $\sim 20 \mu\text{K} (\text{MJy sr}^{-1})^{-1}$ , although higher than the  $0.2 \mu\text{K} (\text{MJy sr}^{-1})^{-1}$  of the translucent cloud LDN 1780, where AME has recently been claimed. The physical properties of the Pleiades nebula, in particular its low extinction  $A_V \sim 0.4$ , indicate that this is indeed a much less opaque object than those where AME has usually been studied. This fact, together with the broad knowledge of the stellar content of this region, provides an excellent testbed for AME characterization in physical conditions different from those generally explored up to now.

*Key words:* cosmic background radiation – diffuse radiation – ISM: individual objects (Pleiades) – radiation mechanisms: general – radio continuum: ISM

*Online-only material:* color figures

### 1. INTRODUCTION

Several microwave experiments, such as *COBE* Differential Microwave Radiometer experiment (Kogut et al. 1996a, 1996b), Owens Valley Radio Observatory (Leitch et al. 1997), Saskatoon (de Oliveira-Costa et al. 1997), 19 GHz (de Oliveira-Costa et al. 1998), or Tenerife (de Oliveira-Costa et al. 1999), have revealed the presence of a statistical correlation between microwave maps and infrared maps tracing the thermal dust emission. These observations motivated a search for similar signals in individual regions (Finkbeiner et al. 2002), which led to unambiguous detections in several molecular clouds with different experiments, such as COSMOSOMAS (Cosmological Structures on Medium Angular Scales; Watson et al. 2005), AMI (Ami Consortium et al. 2009a, 2009b), CBI (Casassus et al. 2006; Castellanos et al. 2011), VSA (Tibbs et al. 2010), or Planck (Planck Collaboration et al. 2011). These studies led to the idea that this dust-correlated signal, which was thenceforth referred to as “anomalous microwave emission” (AME), was indeed an additional diffuse foreground component, originated by an emission mechanism different from the well-known synchrotron, free–free and thermal dust emissions.

AME, which is a significant contaminant of the cosmic microwave background (CMB) in the range  $\sim 20$ – $60$  GHz, was first thought to be free–free emission from  $T_e \gtrsim 10^6$  K gas

(Leitch et al. 1997). This high temperature would be required to reconcile the observed microwave intensity with the lack of intense  $H\alpha$  emission, as it would be expected in the case of bremsstrahlung emission with lower gas temperatures. However, Draine & Lazarian (1998a) ruled out such high temperatures on energetic grounds, and proposed electric dipole emission from small rotating dust grains in the interstellar medium (the so-called *spinning dust*), a mechanism first proposed by Erickson (1957), as a plausible explanation for AME. The models provided by Draine & Lazarian (1998b) for different media show peaked spectra with maximum emissivities at  $\sim 20$ – $50$  GHz which reproduce the observations fairly well (Finkbeiner 2004; de Oliveira-Costa et al. 2004; Watson et al. 2005; Iglesias-Groth 2005, 2006; Casassus et al. 2006, 2008; Dickinson et al. 2009; Tibbs et al. 2010). Recently, the previous analytical models have been refined by different groups by introducing more detailed considerations of the grain shapes and their rotational properties (Ali-Haïmoud et al. 2009; Hoang et al. 2010, 2011; Silsbee et al. 2011).

Draine & Lazarian (1999) presented an alternative explanation for AME based on magnetic dipole radiation from hot ferromagnetic grains. Models of magnetic dipole emission based on single-domain grains, which predict polarization fractions significantly larger than those of the electric dipole emission (Lazarian & Draine 2000), have been ruled out by different

observations (Battistelli et al. 2006; Casassus et al. 2006; Kogut et al. 2007; Mason et al. 2009; López-Caraballo et al. 2011).

Bennett et al. (2003) proposed an alternative mechanism based on a flat-spectrum synchrotron radiation associated with star formation activity to explain *Wilkinson Microwave Anisotropy Probe* (*WMAP*) first-year observations. However, this hypothesis was questioned by other studies. De Oliveira-Costa et al. (2004) argued that the spinning dust hypothesis is clearly favored as it can explain the downturn seen in the dust-correlated signal below 20 GHz (Fernández-Cerezo et al. 2006; Hildebrandt et al. 2007), whereas Davies et al. (2006) found significant correlation in regions away from star-forming regions. More recently, Kogut et al. (2011) have concluded that spinning dust models can fit the *ARCADE* data at 3, 8, and 10 GHz better than the flat-spectrum model.

In this paper, we present a study of the AME arising in the Pleiades reflection nebula, using data at  $\sim 11\text{--}17$  GHz from the *COSMOSOMAS* experiment and at  $\sim 20\text{--}60$  GHz from *WMAP*. This nearby region, having various bright stars capable of exciting the circumstellar medium, is an obvious AME candidate. Its relatively high Galactic latitude ( $b = -24^\circ$ ) also makes it attractive as we can largely avoid contamination from the Galactic plane. Furthermore, it has been widely studied, there being extensive information in the literature about its physical properties that allow us to better understand and to constrain the AME intensities. As we will see next, those studies normally refer to different dust substructures located within this region. However, the low angular resolution ( $\sim 1^\circ$ ) of the microwave data we handle precludes us from studying those individual features, and therefore we will be focused in the whole complex, to which we will refer to as the “Pleiades reflection nebula.”

## 2. PLEIADES ENVIRONMENT AND PHYSICAL CONDITIONS

The discovery of a reflection nebulosity toward the Pleiades star cluster (Tempel 1861) revealed the presence of interstellar dust in this region. This dust is reflecting light from hot blue stars in this cluster, especially the bright stars 17 Tau, 20 Tau, 23 Tau, and 25 Tau, with *B*-band magnitudes ranging from 2.81 to 4.11 (Ritchey et al. 2006) and respective spectral types B6 III, B7 III, B6 IV, and B7 III (White et al. 2001). The Pleiades cluster lies within the Taurus complex at a distance of 125 pc (van Leeuwen 1999), and extends  $\sim 30'$  ( $\sim 1$  pc) around coordinates R.A. =  $3^{\text{h}}46^{\text{m}}$ , decl. =  $23^\circ47'$  (J2000). Castelaz et al. (1987) discovered infrared dust emission around the positions of the Pleiades stars, which they attribute to nonequilibrium very small grains or to molecules with 10–100 carbon atoms. The brightness distribution of this emission, which extends  $\sim 1^\circ$ , and its connection with the exciting stars, can be appreciated in Figure 1, where we show a DSS blue-band image with  $100\ \mu\text{m}$  *IRAS* intensity contours overlaid. The strong emission  $\sim 15'$  south of 23 Tau is originated in the Merope molecular cloud, identified by Federman & Willson (1984) in CO maps. Another two bright knots of infrared emission are seen in the *IRAS* maps concentrated around the stars 17 Tau and 20 Tau.

Except for the area of the Merope molecular cloud, with  $E_{B-V} = 0.35$  mag measured in the direction of the background star HD23512 by White et al. (2001), the optical depth in this region is low ( $E_{B-V} \sim 0.03\text{--}0.07$  mag), and there seems to be little other dust along the cluster line of sight (Cernis 1987). The

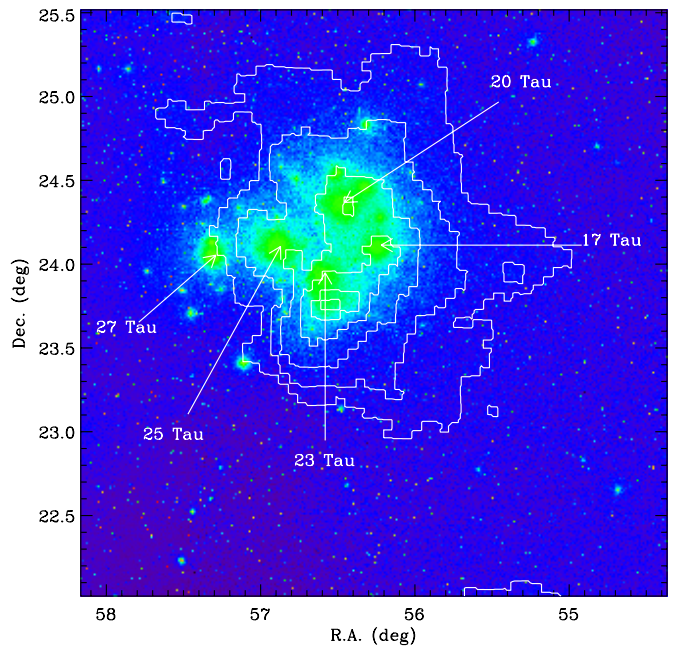


**Figure 1.** Digitized sky survey blue-band photometry ([http://archive.stsci.edu/cgi-bin/dss\\_form](http://archive.stsci.edu/cgi-bin/dss_form)). This image was taken with the Oschin Schmidt 48-inch Telescope on Palomar Mountain.) in the region of the Pleiades star cluster with *IRAS*  $100\ \mu\text{m}$  data overlaid with contours. These contours correspond to intensity levels of 20, 30, 50, 100, 200, and  $300\ \text{MJy sr}^{-1}$ . Arrows point to the positions of the main exciting stars in the region, and the circle indicates the aperture we will use for flux integration.

(A color version of this figure is available in the online journal.)

physical properties of the gas in different positions of the whole complex have been studied by different authors. Federman & Willson (1984) obtained gas densities  $n \sim 300\text{--}500\ \text{cm}^{-3}$  and temperatures  $T_g \sim 20$  K from molecular line observations in the Merope molecular cloud. They found column densities intermediate between diffuse and dark clouds, and concluded that Merope is indeed much less opaque than typical Taurus clouds. White (1984) studied a larger area in the Pleiades enclosing the main exciting stars and estimated densities  $n \sim 400\ \text{cm}^{-3}$ , whereas Gordon & Arny (1984) found  $n \sim 100\ \text{cm}^{-3}$  in a similar area. Ritchey et al. (2006) obtained even lower values of  $n \sim 46, 16$ , and  $40\ \text{cm}^{-3}$  in the lines of sight of 25 Tau, 27 Tau, and 28 Tau, respectively.

Different studies, based on CO maps (Federman & Willson 1984) and on high-resolution spectra toward Pleiades stars (White 2003), have shown the gas and dust that make up the Pleiades nebula to have a significant radial velocity offset relative to the star cluster. A corollary of this is that the Pleiades stars were not formed out of this surrounding material but, more likely, the spatial association between the stars and the interstellar gas is the result of a chance encounter between the cluster and one or more approaching clouds. White (1984) identified two separated phases: one layer of atomic gas with (local standard of rest) a radial velocity of  $7\ \text{km s}^{-1}$ , lying  $\gtrsim 1$  pc in front of the cluster and with a thickness of  $\lesssim 0.3$  pc, and one molecular phase (though strongly ionized) with a radial velocity of  $10\ \text{km s}^{-1}$  within the cluster. The presence of these two phases was confirmed by latter studies, which also showed that the atomic phase probably belongs to the Taurus clouds, but are inconclusive on whether or not the molecular phase is embedded within the star cluster (White 2003; Gibson & Nordsieck 2003).

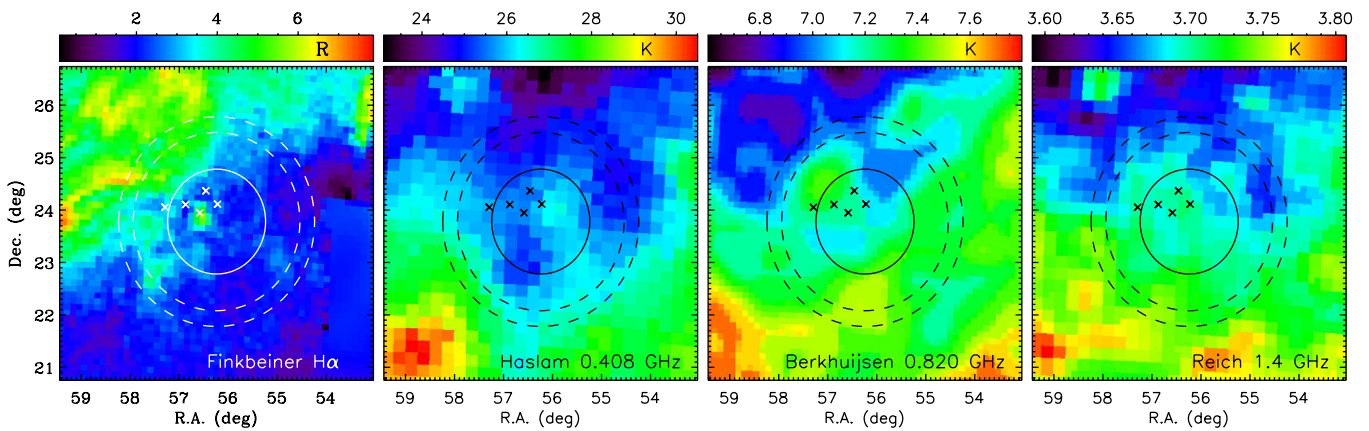


**Figure 2.**  $H\alpha$  intensity and radio temperature maps in the position of the Pleiades reflection nebula. Crosses mark the positions of the same stars as shown in Figure 1. A small knot of  $H\alpha$  emission is seen  $\sim 10'$  south of 23 Tau, but in the radio maps its associated free-free emission is overshadowed by the noise and background fluctuations.

(A color version of this figure is available in the online journal.)

### 3. DATA ANALYSES

#### 3.1. Expected Free-Free Emission from $H\alpha$

The radio free-free emission must be accurately characterized in order to quantify any possible dust-correlated excess at microwave frequencies. To this end, we follow the method described in Dickinson et al. (2003), which allows to estimate the level of this emission from  $H\alpha$ . We resort to the full-sky  $H\alpha$  map compiled by Finkbeiner (2003), a patch of which is shown in Figure 2 in the region of the Pleiades reflection nebula. The solid circle depicts the  $1^\circ$  aperture we will use in this work for flux integration, while the area limited by the two dashed circles at radii  $1^\circ 7$  and  $2^\circ 0$  defines the annulus where we will average the background signal that will be subtracted. However, in this case it is evident that this annulus would not give a reliable estimation of the background, as it contains clear contaminant signal rather different from the true background level around the Pleiades clouds. In fact, the averaged signal is larger in the background annulus than in the aperture, giving a negative background-subtracted  $H\alpha$  intensity of  $-0.41 \pm 0.09$  R. When positioning the background annulus at different radii between  $1^\circ 0$  and  $3^\circ 0$  we consistently get negative values between  $\approx -0.2$  R and  $\approx -0.6$  R. Therefore, from an aperture integration here we can only set upper limits on the  $H\alpha$  emission. Instead, we choose to proceed in a different way.

Inside the aperture the only evident signal above the background level is a bright  $H\alpha$  knot located  $\sim 10'$  south of 23 Tau and coincident with the position of the Merope molecular cloud. On these grounds we consider that all the  $H\alpha$  emission associated with the Pleiades nebula is produced in this position. In order to calculate its associated intensity we fit this feature with a two-dimensional elliptical Gaussian function plus a constant background level. We obtain a maximum amplitude (source plus background) of 5.90 R, a background level of 2.58 R, and an FWHM of  $14/3$  and  $20/7$  in two orthogonal directions. Using these parameters the mean background-subtracted  $H\alpha$  intensity in the aperture is  $I_{H\alpha} = 0.092$  R. Note that this value is higher than the  $3\sigma$  upper limit obtained through aperture photometry. Therefore, it is more conservative, as it will be extrapolated to microwave frequencies in order to characterize any possible excess emission in that range.

This value needs correction from Galactic extinction,  $I_{H\alpha}^{\text{corr}} = I_{H\alpha} \times 10^{A(H\alpha)/2.5}$ . Using O'Donnell (1994) polynomials that

allow calculating the extinction at any given wavelength in the range  $\sim 0.3\text{--}0.9 \mu\text{m}$ , and taking  $R_V = A_V/E_{B-V} = 3.6$  from Cernis (1987), we obtain  $A(H\alpha) = 2.94E_{B-V}$ . Ideally we should apply a pixel-by-pixel correction, for which we would need a reddening map. We have inspected the Schlegel et al. (1998) full-sky  $E_{B-V}$  map in this region, which gives a mean reddening inside the aperture of 0.30 mag, with a maximum of 2.06 mag in a position  $\sim 15'$  south of 23 Tau, coincident with the Merope molecular cloud. Ritchey et al. (2006) give reddening values toward 20 stars belonging to the Pleiades (taken from White et al. 2001), with an average value of 0.074 mag, and a maximum of 0.35 mag toward the star HD23512. These figures are consistent with other measurements in the direction of Pleiades or background stars (White 1984; Cernis 1987; Herbig & Simon 2001). The reddenings from the Schlegel et al. (1998) map correspond to the full integral along the line of sight, and therefore their higher values could be due to the extinction produced in background dust. However, given the relatively high Galactic latitude of the Pleiades, one would expect those differences to be smaller. Therefore, instead of performing a pixel-by-pixel correction, we conservatively assume an average value of  $E_{B-V} = 0.1$ , which is slightly larger than the mean over the 20 stars of Ritchey et al. (2006). We finally obtain  $I_{H\alpha}^{\text{corr}} = 0.12$  R, and assuming an electron temperature of 8000 K, we obtain an emission measure (EM) of  $\text{EM} = 0.267 \text{ cm}^{-6} \text{ pc}$ . From this, we derive the expected spectrum of free-free flux integrated over the aperture.

#### 3.2. Radio Data

There are different radio surveys from which we can also constrain the free-free emission. We use the Haslam et al. (1982) map at 0.408 GHz,<sup>5</sup> the Berkhuijsen (1972) map at 0.820 GHz,<sup>6</sup> and the Reich & Reich (1986) map at 1.4 GHz.<sup>7</sup> These maps smoothed to a common resolution of  $1^\circ$  (except the 0.820 GHz map, whose original resolution is  $1^\circ 2$ ) in the position of the Pleiades are shown in Figure 2. No obvious excess above the background and noise levels is seen, so we have to establish

<sup>5</sup> We use the map supplied by Platania et al. (2003).

<sup>6</sup> Downloaded from <http://www.mpifr-bonn.mpg.de/survey.html>

<sup>7</sup> These maps (and, in general, all used in this work) are projected into the HEALPix (Górski et al. 2005) pixelization scheme, using a pixel size of  $\sim 7'$  ( $N_{\text{side}} = 512$ ). In the case of the 0.820 GHz data we carried out the repixelization ourselves, as they are given in a different format.

**Table 1**  
Fluxes and Dust-correlated Emissivities

$\nu$ (GHz)	Case A			Case B		
	Flux (Jy)	Residual Flux (Jy)	Correlation $\mu\text{K (MJy sr}^{-1})^{-1}$	Flux (Jy)	Residual Flux (Jy)	Correlation $\mu\text{K (MJy sr}^{-1})^{-1}$
0.408	<1.14	<1.11	...	<1.14	<1.11	...
0.820	<0.89	<0.87	...	<0.89	<0.87	...
1.42	<0.51	<0.49	...	<0.51	<0.49	...
10.9	<1.04	<0.87	...	<0.94	<0.91	...
12.7	<1.97	<1.75	...	<1.83	<1.80	...
14.7	<1.77	<1.48	...	<1.58	<1.56	...
16.3	<2.43	<2.08	...	<2.20	<2.17	...
22.8	$2.60 \pm 0.06 (\pm 0.51)$	$1.95 \pm 0.06$	$3.01 \pm 0.27$	$2.15 \pm 0.12$	$2.12 \pm 0.12$	$4.36 \pm 0.17$
33.0	$2.55 \pm 0.10 (\pm 1.06)$	$1.21 \pm 0.12$	$0.66 \pm 0.17$	$1.61 \pm 0.15$	$1.55 \pm 0.15$	$2.01 \pm 0.09$
40.7	$2.64 \pm 0.15 (\pm 1.59)$	$0.64 \pm 0.17$	$-0.32 \pm 0.16$	$1.24 \pm 0.18$	$1.12 \pm 0.18$	$1.03 \pm 0.03$
60.8	$4.71 \pm 0.36 (\pm 3.37)$	$0.39 \pm 0.40$	$-0.77 \pm 0.16$	$1.75 \pm 0.38$	$1.23 \pm 0.38$	$0.59 \pm 0.02$
93.5	$9.12 \pm 0.89 (\pm 7.03)$	$-0.52 \pm 0.97$	$-0.25 \pm 0.12$	$2.94 \pm 0.90$	$0.37 \pm 0.90$	$1.10 \pm 0.05$
1249.1	$11931 \pm 185$	$9 \pm 394$	...	$11931 \pm 185$	$-366 \pm 195$	...
2141.4	$23469 \pm 249$	$-14 \pm 595$	...	$23469 \pm 249$	$618 \pm 262$	...
2997.9	$17959 \pm 89$	$1 \pm 375$	...	$17959 \pm 89$	$-47 \pm 101$	...

**Notes.** Flux upper limits at the 99.7% C.L. level are shown for the 0.408–1.42 GHz and COSMOSOMAS (10.9–16.3 GHz) data. For *WMAP* and DIRBE frequencies fluxes are obtained through an aperture integration, using a radius of  $1^\circ$  for the aperture and subtracting a mean background calculated in an annulus between  $1^\circ.7$  and  $2^\circ.0$  around the source. The fluxes on the right (case B) were calculated on maps where a pixel-by-pixel subtraction of a CMB ILC map was applied. The error bars include instrumental noise, and the numbers within brackets show errors associated with the CMB anisotropies. The residual fluxes represent the level of AME, as they were obtained after the subtraction of the rest of the modeled components. We also show the dust-correlated emissivities, which indicate the correlation between *WMAP* and the *IRAS* 100  $\mu\text{m}$  map.

upper limits for the flux densities at these frequencies. To this end, we assume the noise per pixel to be equal to the standard deviation of the signal calculated in the background region (external annulus) of the maps smoothed to  $1^\circ$ . The flux noises in the aperture derived from this assumption are, respectively, 0.38, 0.30, and 0.17 Jy (68% confidence level (C.L.); in Table 1 we show upper limits at the 99.7% C.L.), while the free-free fluxes estimated from  $\text{H}\alpha$  (see the previous section) at those frequencies are at a level of  $\sim 0.030\text{--}0.027$  Jy.

### 3.3. Microwave Data

#### 3.3.1. COSMOSOMAS

The COSMOSOMAS experiment consisted of two circular-scanning instruments, the so-called COSMO11 and COSMO15, operative between 1998 and 2008 from the Teide Observatory (altitude 2400 m, Tenerife). They produced  $0^\circ.8\text{--}1^\circ.1$  resolution daily maps with full coverage in right ascension and  $\sim 20^\circ$  coverage in declination in four frequency bands centered at 10.9 GHz for COSMO11, and 12.7, 14.7, and 16.3 GHz for COSMO15. A description of the instrumental setup of COSMO11 and COSMO15 can be found in Hildebrandt et al. (2007) and Gallegos et al. (2001), respectively.

An important step of the data processing is the removal of the first seven harmonics of each scan, in order to suppress the  $1/f$  noise from the receiver and from the atmosphere. Each scan, which is a stack of 30 s of data (corresponding to 30 spins of the primary mirror), is Fourier-fitted and terms up to seventh order (i.e., a constant term plus seven sin and cos terms) are removed. This results in a distortion of the broad angular scales and in a loss of flux. Further details on the data reduction, calibration, and map-making of COSMO11 and COSMO15 data can be found in Hildebrandt et al. (2007) and in Fernández-Cerezo et al. (2006), respectively. In those references the final maps can be seen, as well as the discussion about the dust-correlated signal that was found at  $|b| > 20^\circ$ .

The maps we use here are a stack of  $\sim 150$  days of observations in each of the two linear polarization modes of COSMO11 (2003 November to 2005 June) and of  $\sim 110$  days of COSMO15 data (1999 October to 2000 January). They are convolved to a common resolution of  $1^\circ.12$ , and have final sensitivities (averaged over the  $\approx 10,000$  deg $^2$  observed sky region) of  $35 \mu\text{K beam}^{-1}$  for COSMO11, and 53, 56, and  $118 \mu\text{K beam}^{-1}$  for the three frequencies of COSMO15.

COSMO11 and COSMO15 observed in different configurations, covering different declination ranges. The minimum declination was  $\approx 23^\circ.5$ . In the case of COSMO15, there are also  $\sim 5$  days in a configuration down to decl. =  $16^\circ.7$ , but we discard these data because they are too noisy. Most of the area encompassed by the Pleiades reflection nebula is covered by the observations, but unfortunately its center lies just  $17'$  from the border of the map. Also, the total number of days of observations in the configurations reaching these low declinations is  $\sim 95$  for COSMO11 and  $\sim 12$  for COSMO15. However, despite the fewer observing days, the map's sensitivities in the region of the Pleiades are similar to the full-map average sensitivities quoted above thanks to the circular scanning strategy, which results in a better spatial coverage toward the edge of the map. Possible edge effects arising in this region are avoided by ignoring the blank pixels in the convolution process.

COSMOSOMAS maps in the region of the Pleiades are shown in Figure 3. No clear detection is seen in any of the frequency bands. Marginal evidence for a weak signal in the position of the Pleiades could be claimed in the COSMO11 map. We obtain an indirect estimate of  $0.67 \pm 0.09$  Jy for the 11 GHz flux from the DIRBE fluxes calculated in Section 3.4 by using the dust-correlated emissivities between the COSMO11 map and the DIRBE 100, 140, and  $240 \mu\text{m}$  maps. However, we conservatively establish flux upper limits for COSMO11 and for the three COSMO15 frequencies, which will in turn be important to trace the AME flux downturn at lower frequencies predicted by spinning-dust models. To this end, we measure the

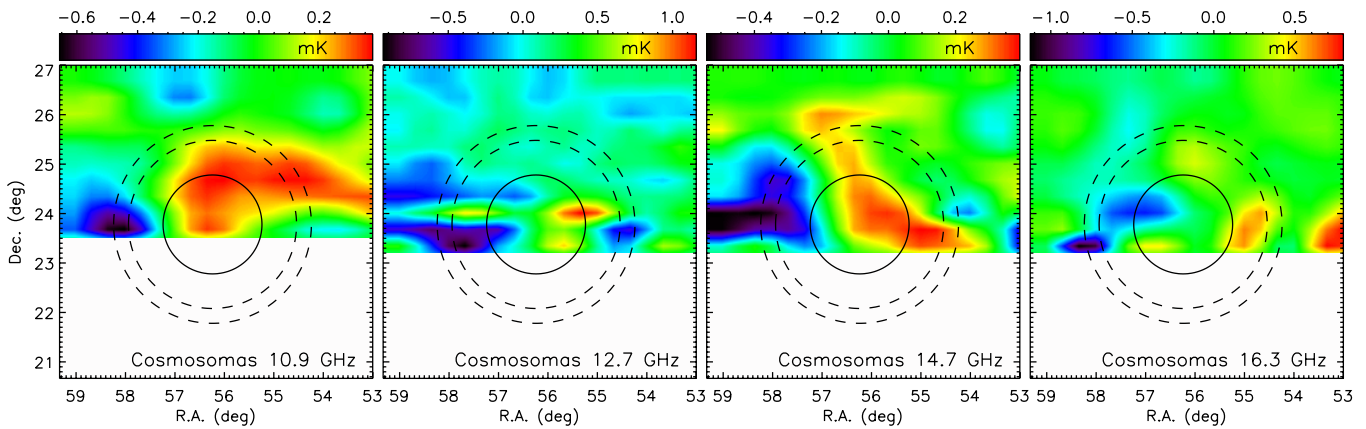


**Figure 3.** COSMOSOMAS maps toward the Pleiades reflection nebula, for the four frequencies of this experiment. Note that here we are displaying data down to a declination of  $\approx 23^\circ 5'$ . There are data in a different configuration which extends the declination coverage to  $16^\circ 7'$ , but with  $\sim 20$  times less integration time, and therefore with a notably higher noise level.

(A color version of this figure is available in the online journal.)

standard deviation in each map within a box of  $\approx 10 \text{ deg}^2$  around the Pleiades, obtaining 65, 96, 65, and  $72 \mu\text{K beam}^{-1}$  for 10.9, 12.7, 14.7, and 16.3 GHz, respectively. After transforming into flux, these values are corrected for the flux suppression caused by the COSMOSOMAS map-making strategy described above. To this end, we simulate a source with the same brightness distribution as the  $100 \mu\text{m}$  DIRBE map in the position of the Pleiades, and a flux normalized to 1 Jy. This source is then degraded to an angular resolution of  $1^\circ 12'$  and convolved with the simulated circular scanning strategy of COSMOSOMAS, which includes removal of the first seven harmonics. By measuring the flux in this final map and comparing with the initial flux of 1 Jy, we conclude that the flux losses are 62% and 66%, respectively, for COSMO11 and COSMO15. Final upper limits are listed in Table 1 at the 99.7% C.L.

### 3.3.2. WMAP Intensity

NASA's *WMAP* satellite has produced full-sky maps at frequency bands centered at 22.8, 33.0, 40.7, 60.8, and 93.5 GHz (*K*, *Ka*, *Q*, *V*, and *W*), and with angular resolutions of  $0^\circ 85'$ ,  $0^\circ 65'$ ,  $0^\circ 51'$ ,  $0^\circ 35'$ , and  $0^\circ 25'$ , respectively. We use the seven-year data products (Jarosik et al. 2011) available in the LAMBDA database.<sup>8</sup> In Figure 4 we represent a composition of the *K*-band map at the position of the Pleiades, with *IRAS*  $100 \mu\text{m}$  contours overplotted, showing an evident spatial correlation between both maps. The Pearson correlation coefficient calculated between maps at the same angular resolution ( $1^\circ$ ) is  $r = 0.608$ . However, the center of the microwave emission seems to be shifted  $\sim 15'$  to the southwest of the position of the stars 23 Tau and 17 Tau, around which the bulk of the infrared emission is seen. Figure 5 shows *WMAP* smoothed maps subtracted from the CMB contribution (see the next paragraph). AME shows up prominently especially in the *K* band. The bulk of the emission, which extends  $\sim 1^\circ 5'$ , seems to be mounted on a larger scale diffuse structure which elongates toward the southwest of the maps. Some emission is also hinted at in the 0.408–1.4 GHz maps (see Figure 2). We calculate spectral indices between 0.408 and 22.8 GHz in different circular apertures on this diffuse region surrounding the Pleiades nebula, obtaining values around  $-0.5$ , which are compatible with synchrotron emission. However, we cannot draw a firm conclusion about the possible

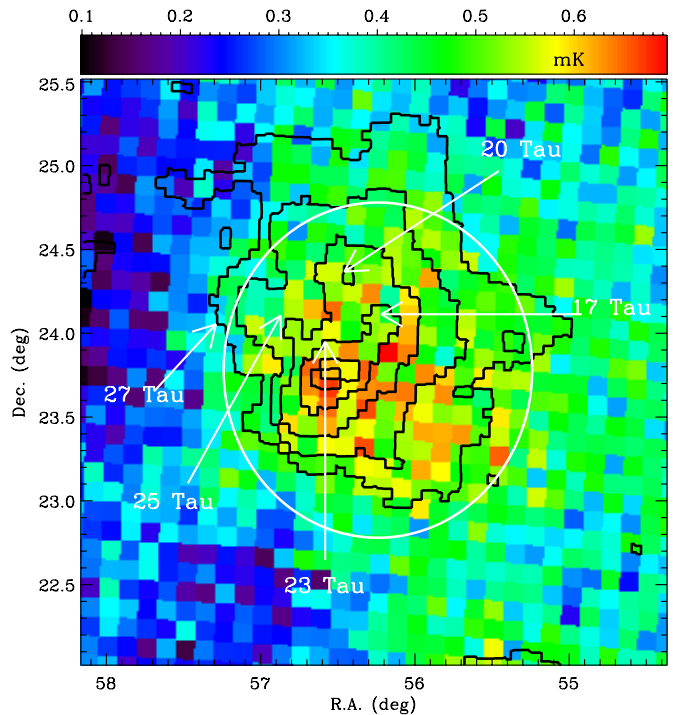


**Figure 4.** *WMAP* *K*-band (22.8 GHz) map with *IRAS*  $100 \mu\text{m}$  data overplotted with contours, in the position of the Pleiades nebula. Arrows indicate the positions of the brightest stars in the region, and the circle the  $1^\circ$  radius aperture we use for flux integration. Temperature units of the *WMAP* map are indicated in the color scale at the top. *IRAS* contours correspond to intensity levels of 20, 30, 50, 100, 200, and  $300 \text{ MJy sr}^{-1}$ . A clear correlation is seen between the microwave (AME) and the infrared (thermal dust emission) intensities.

(A color version of this figure is available in the online journal.)

contribution from AME owing to the low flux density and to the contamination from the stronger emission arising within the Pleiades dust. Radial profiles of the *WMAP* *K*-band map at its original angular resolution across the source in different directions show the 22.8 GHz emission to extend  $\sim 1^\circ$ , being slightly resolved by the  $0^\circ 85'$  FWHM beam. This further supports the hypothesis that, even if the bulk of the microwave emission may be coming from a position  $\sim 15'$  southwest of 23 Tau and 17 Tau, there may be an important diffuse component originating in a wider region encompassing this nebulousity.

<sup>8</sup> <http://lambda.gsfc.nasa.gov/>

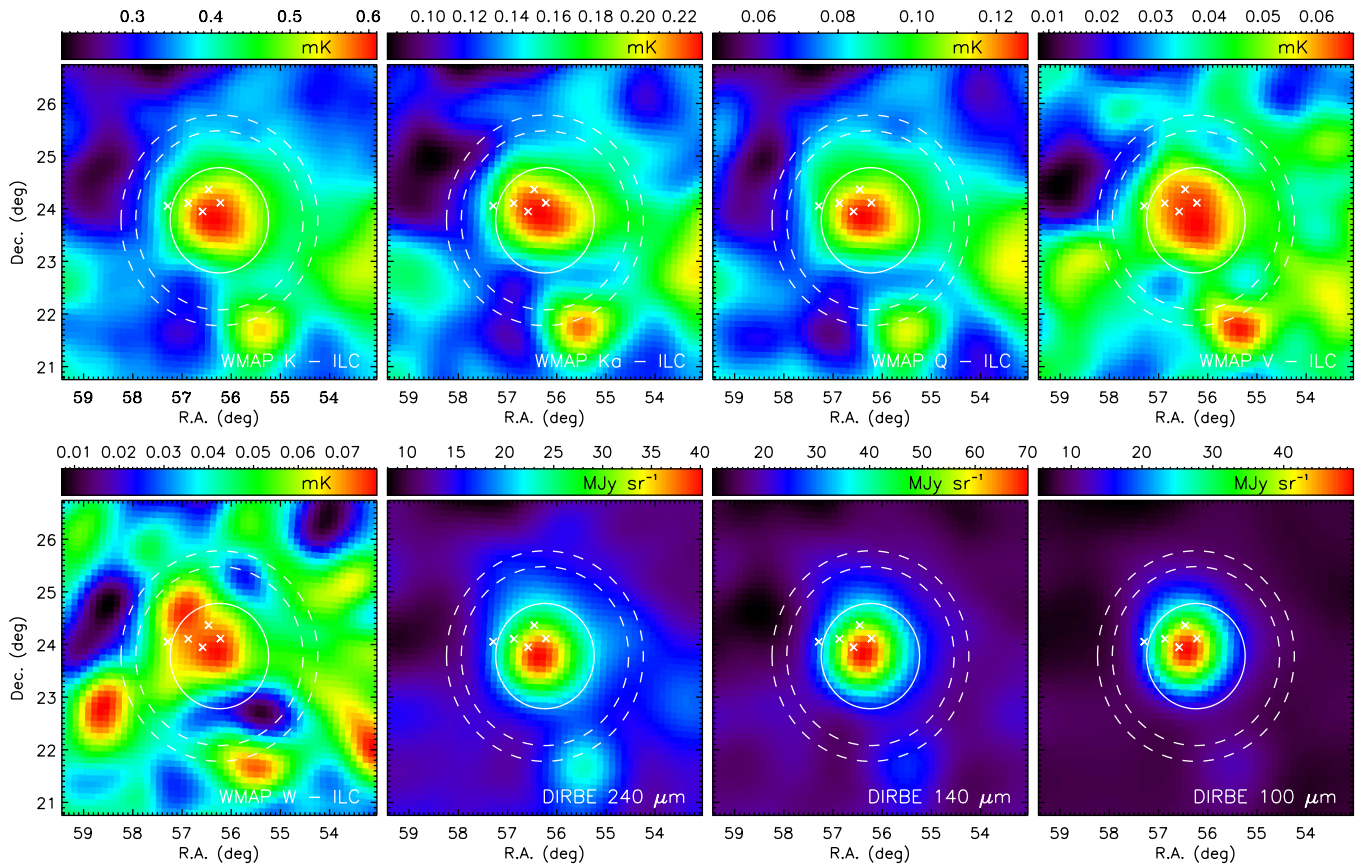


**Figure 5.** *WMAP* and DIRBE maps smoothed to a common resolution of  $1^\circ$ . *WMAP* maps have been subtracted from the CMB contribution given by the ILC template (see the text for details). Crosses mark the positions of the same stars as shown in Figure 1. The  $1^\circ$  radius circular aperture and  $1.7$ – $2.0^\circ$  circular annulus which are used for flux extraction are indicated. Strong AME is evident in *WMAP* maps, with maximum intensity at 22.8 GHz.

(A color version of this figure is available in the online journal.)

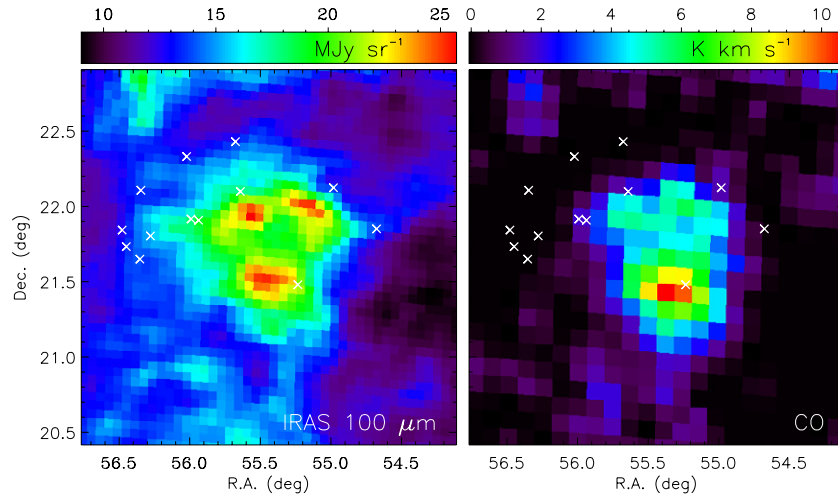


**Figure 6.** *IRAS*  $100\ \mu\text{m}$  and CO maps of the source found toward the southwest of the Pleiades, with coordinates (R.A., decl.) =  $55^\circ44' + 21^\circ67'$ . Crosses mark the positions of the infrared sources from the *IRAS* catalog.

(A color version of this figure is available in the online journal.)

Toward the southwest of the Pleiades stars, at equatorial coordinates (R.A., decl.) =  $55^\circ44' + 21^\circ67'$ , *WMAP* maps also reveal a source, with a flux of  $\approx 0.6$  Jy at 22.8 GHz, which has no counterpart in the 1.4 GHz NVSS (Condon et al. 1998) nor in the *WMAP* point-source catalogs (Gold et al. 2011). It does not have significant emission in the 0.408–1.4 GHz maps nor in the H $\alpha$  map of Finkbeiner (2003). The flux upper limits that can

be derived from the radio data, and the flux value at 22.8 GHz, are consistent with a free–free spectrum. *WMAP* 93.5 GHz data show evidence of thermal dust emission. Moreover, as is shown in Figure 6, this source is visible in *IRAS* 60 and  $100\ \mu\text{m}$  maps as a circular ring with a diameter of  $\approx 40'$ , as well as in the CO map of Dame et al. (2001). There are several infrared sources around that position listed in the *IRAS* point-source catalog. The

spectrum of *WMAP* and DIRBE data is compatible with thermal dust emission.

For the sake of consistency, we perform the flux extraction in maps at the same angular resolution. We then use LAMBDA maps degraded to a common resolution of  $1^\circ$ . Onward we will consider two separate strategies for flux calculation: (1) case A: we apply our method for flux extraction directly on those maps, which may contain some CMB contamination; (2) case B: we construct CMB-subtracted maps on which our method for flux extraction will be applied. To define the CMB template that will be pixel-by-pixel subtracted from the original maps, rather than using the full-sky internal linear combination (ILC) map supplied by the *WMAP* team, we generate our own ILC in a circular area of  $30^\circ$  radius around the Pleiades after masking out point sources by applying *WMAP*'s KQ85 mask. We use the same technique as the *WMAP* team, i.e., a weighted linear combination of the five smoothed frequency maps, in which the weights are chosen to minimize the variance of the measured temperatures, in order to maintain the CMB contribution while minimizing the foreground contribution. Pixel temperatures in our ILC are given by  $T_{\text{ILC}} = -0.1937T_K - 0.0550T_{\text{Ka}} + 0.8289T_Q + 0.7042T_V - 0.28437T_W$ , and the resulting CMB-subtracted maps are shown in Figure 5.

In order to extract the fluxes we use a direct aperture integration. This is a well-known technique (Bennett et al. 1993; Hernández-Montegudo & Rubiño-Martín 2004; Planck Collaboration et al. 2011), consisting of integrating temperatures of all pixels within a given aperture and subtracting a background level which is calculated by averaging pixel temperatures enclosed by an external annulus. The flux is then given by

$$S_\nu = a(\nu) \left[ \frac{\sum_{i=1}^{n_1} T_i}{n_1} - \frac{\sum_{j=1}^{n_2} T_j}{n_2} \right], \quad (1)$$

where  $n_1$  and  $n_2$  are, respectively, the number of pixels in the circular aperture and in the external annulus, and  $T_i$  and  $T_j$  represent the pixel thermodynamic temperatures in the aperture and in the background annulus. The function  $a(\nu)$  gives the conversion factor from temperature to flux,

$$a(\nu) = \frac{h^2 \nu^4}{2k_b T_{\text{cmb}}^2 c^2} \sinh^{-2} \left( \frac{h\nu}{2k_b T_{\text{cmb}}} \right) n_1 \Omega_{\text{pix}}, \quad (2)$$

where  $h$  and  $k_b$  are the Planck and Boltzmann constants,  $T_{\text{cmb}} = 2.725$  K (Mather et al. 1999) is the CMB temperature, and  $\Omega_{\text{pix}}$  is the solid angle subtended by each pixel. The associated error bar is calculated through the quadratic sum of the variance of each pixel (given by *WMAP* error maps) plus the pixel-to-pixel covariance:

$$\sigma(S_\nu) = a(\nu) \left[ \frac{1}{n_1^2} \left( \sum_{ij}^{n_1 n_1} C(\theta_{ij}) + \sum_i^{n_1} \sigma_i^2 \right) + \frac{1}{n_2^2} \left( \sum_{ij}^{n_2 n_2} C(\theta_{ij}) + \sum_i^{n_2} \sigma_i^2 \right) - \frac{2}{n_1 n_2} \sum_{ij}^{n_1 n_2} C(\theta_{ij}) \right]^{1/2}. \quad (3)$$

In this equation  $\sigma_i$  represents the instrumental noise associated with each pixel.  $C(\theta_{ij})$  is the noise correlation function, which arises from the smoothing process, and is evaluated for any pair of pixels separated by an angle  $\theta_{ij}$ . For case A, we also calculate

the error associated with the CMB primordial fluctuations, by introducing its correlation function, derived from a theoretical power spectrum obtained from the *WMAP* best-fit cosmological model.

The radii we use for the aperture and for the internal and external circles defining the annulus are shown in Figure 5. These are, respectively,  $1^\circ$ ,  $1^\circ 7'$ , and  $2^\circ 0'$ , and were chosen from the radial angular profiles of the signal. These angular profiles flatten at the distance of the background annulus, and the aperture encloses the bulk of the microwave and infrared emissions associated with the Pleiades. The center coordinates of the aperture are R.A. =  $3^{\text{h}}44^{\text{m}}58^{\text{s}}$ , decl. =  $23^\circ 46' 48''$  (J2000). This position is chosen to match the maximum emission at 22.8 GHz, and is located  $\approx 15'$  southwest of the middle of the line connecting the 17 Tau and 23 Tau stars, around which the bulk of the infrared emission is located. Final fluxes are shown in Table 1. Error bars include only the thermal noise, and the contribution from the CMB variance is indicated within brackets for case A. In case B the flux error bar includes the ILC noise, which is calculated in each map pixel through the quadratic sum of pixel noises for all bands weighted by the corresponding ILC coefficient. The flux at 22.8 GHz calculated in the ILC map, which is subtracted in case B, is  $0.45 \pm 0.11$  Jy. This value is compatible with 0.51 Jy, which corresponds to the standard deviation of the CMB primordial fluctuations associated with this measurement.

At 22.8 GHz we get  $2.15 \pm 0.12$  Jy for case B, which is two orders of magnitude above the level of free-free emission at this frequency derived from H $\alpha$  (0.02 Jy; see Section 3.1). We will see later in Section 4 that this flux is in fact dominated by AME, as the contribution from thermal dust emission is rather low at this frequency. Also, considering the upper limit from COSMO11, the spectral index between 10.9 and 22.8 GHz is  $\beta_{11-23} \gtrsim 1.12$ , a value consistent with typical spinning dust models.

### 3.3.3. *WMAP* Polarization

Estimates or constraints of the AME polarization can help to discriminate between models based on electric dipole emission from very small spinning dust grains and magnetic dipole radiation from hot ferromagnetic grains (see Section 1 and references therein). It is therefore interesting to obtain estimates of the polarization from *WMAP* maps of  $Q$  and  $U$  Stokes parameters. Applying the same aperture photometry technique as in Section 3.3.2 in these maps, which show no significant emission at the position of the Pleiades, we get fluxes of  $Q = 0.076 \pm 0.071$  Jy and  $U = -0.056 \pm 0.091$  Jy at 22.8 GHz. Using these values, together with the flux density for case B (see the previous section), we derive a 95% C.L. upper limit on the polarization fraction,  $\Pi = \sqrt{Q^2 + U^2}/I$ , of  $\Pi < 10.8\%$ . This constraint is much weaker than  $\Pi < 1.0\%$  obtained in the much brighter region of the Perseus molecular cloud (López-Caraballo et al. 2011).

### 3.4. Far-infrared Data

Far-infrared data trace the thermal dust emission, which can then be extrapolated to microwave frequencies. We use Zodi-Subtracted Mission Average *COBE*-DIRBE maps (Hauser et al. 1998) at  $240 \mu\text{m}$  (1249 GHz),  $140 \mu\text{m}$  (2141 GHz), and  $100 \mu\text{m}$  (2998 GHz). Although there are DIRBE data at higher frequencies, we consider these three bands only, because they allow modeling of the thermal dust spectrum with a

single modified blackbody curve. Higher frequency bands are dominated by a different grain population and their inclusion would make at least two curves necessary. We also note that, in spite of *IRAS* finer angular resolution, we use DIRBE data here because the *IRAS* lower frequency band is  $100\ \mu\text{m}$ , and also because we calculate fluxes in a larger angular scale than either of the *IRAS* and DIRBE beam sizes.

In Figure 5 we show the DIRBE maps at the position of the Pleiades smoothed to a resolution of  $1^\circ$ . It is again clear from these plots that the microwave emission is slightly shifted to the southwest with respect to the infrared emission at  $100\ \mu\text{m}$ . This offset is less pronounced at  $140\ \mu\text{m}$ , and almost disappears at  $240\ \mu\text{m}$ . The Pearson correlation coefficients between *WMAP* 22.8 GHz and DIRBE bands from  $100\ \mu\text{m}$  to  $240\ \mu\text{m}$  are, respectively,  $r = 0.585$ ,  $0.722$ , and  $0.821$ . However, our aperture encloses the bulk of the flux in both frequency ranges. Aperture-photometry fluxes in the three bands are quoted in Table 1. We also show the dust-correlated emissivities, which are used to quantify the correlation between the  $100\ \mu\text{m}$  DIRBE map and *WMAP* maps. These are calculated by a linear fit of the temperature ( $\mu\text{K}$ ) of *WMAP* background-subtracted pixels to the intensity ( $\text{MJy sr}^{-1}$ ) of DIRBE background-subtracted pixels using a standard least-squares method. A significant correlation is found, specially between *WMAP* 22.8 GHz and DIRBE  $100\ \mu\text{m}$  channels, where we get  $4.36 \pm 0.17\ \mu\text{K} (\text{MJy sr}^{-1})^{-1}$ . We note however that this dust emissivity is strikingly lower than those obtained in dust clouds (Davies et al. 2006), which usually range from  $\sim 11$  to  $\sim 35\ \mu\text{K} (\text{MJy sr}^{-1})^{-1}$ , and more similar to  $3.3 \pm 1.7\ \mu\text{K} (\text{MJy sr}^{-1})^{-1}$  found by Dickinson et al. (2007) in H II regions. Vidal et al. (2011) obtained an even lower value of  $0.2 \pm 0.1\ \mu\text{K} (\text{MJy sr}^{-1})^{-1}$  in the translucent cloud LDN 1780, where they found evidence of AME.

#### 4. SPECTRAL ENERGY DISTRIBUTION

Figures 7 and 8 depict the spectral energy distributions (SEDs) for cases A and B, respectively. In both cases, we represent  $3\sigma$  (99.7% C.L.) upper limits at 0.408, 0.820, and 1.42 GHz, as no significant emission was found at these frequencies (see Section 3.2). Upper limits at the 99.7% C.L. are also shown for COSMO11 and for the three channels of COSMO15 (see Section 3.3.1).

AME, which neatly shows up in the SEDs as a bump at frequencies  $\sim 20$ – $60$  GHz, is usually well fitted by spinning-dust models (see Section 1 and references therein). Following Planck Collaboration et al. (2011), we consider two complementary spinning-dust components, corresponding, respectively, to high-density molecular gas and low-density atomic gas. Different studies of the dynamics of the Pleiades environment agree on the existence of these two gas phases, the former being probably located within the cluster and the latter lying  $\sim 1$  pc in front of it (see Section 2 and references therein). We compute spinning-dust emissivities per hydrogen column density of these two phases using the `SPDUST.2` code<sup>9</sup> (Ali-Haïmoud et al. 2009; Silsbee et al. 2011). Rather than fitting all the spinning dust parameters to the observed spectra, we use realistic values and fit the amplitude to the spectrum. Assumed physical parameters for these two phases, which are used as inputs for `SPDUST.2`, are shown in Table 2.  $n_{\text{H}}$  is the total hydrogen number density,  $T_{\text{g}}$  is the kinetic gas temperature,  $\chi$  is the intensity of the radiation field relative to the average interstellar radiation field,  $x_{\text{H}} = n_{\text{H}}^+ / n_{\text{H}}$  represents the hydrogen ionization fraction,  $x_{\text{C}} = n_{\text{C}}^+ / n_{\text{H}}$

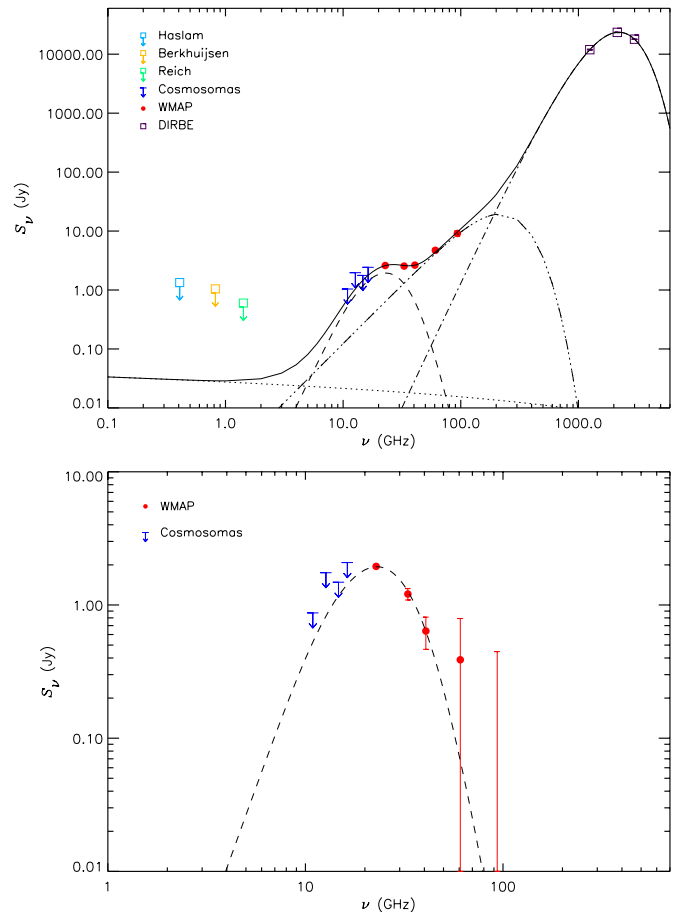


**Figure 7.** Top: SED of the Pleiades nebula for case A. Upper limits are shown at the 99.7% C.L. for radio and COSMOSOMAS data. *WMAP* and DIRBE fluxes have been obtained through aperture photometry, and are quoted in Table 1. The fitted model consists of free–free emission (dotted line), thermal dust (dash-dotted line), CMB (dash-triple-dotted line), and a spinning dust model for a molecular gas phase (dashed line). The model parameters are listed in Table 2. Bottom: residual SED after subtraction of the free–free and the best-fit CMB and thermal dust components.

(A color version of this figure is available in the online journal.)

the ionized carbon fractional abundance,  $y = 2n(\text{H}_2)/n_{\text{H}}$  the molecular hydrogen fractional abundance, and  $\beta$  represents the average dipole moment per atom. Parameters for the grain-size distribution are taken from line 25 of Table 1 of Weingartner & Draine (2001).

Different studies of the Pleiades interstellar material cited in Section 2 provide temperatures around  $T_{\text{g}} \sim 20$  K and densities spanning from  $n \sim 40\ \text{cm}^{-3}$  (Ritchey et al. 2006) to  $\sim 400\ \text{cm}^{-3}$  (White 1984). This allows flexibility when fixing our model parameters. Moreover, we note that some of the aforementioned studies focused on individual clouds whereas here we study the emission integrated over an area encompassing the whole Pleiades reflection nebula. The physical parameters we choose for the molecular phase are similar to those of the molecular cloud environment of Draine & Lazarian (1998b), while those of the atomic phase have been adapted to have a spectrum peaking at a higher frequency, in order to provide a better fit to the 60.8 GHz point. The position of the peak of the spinning dust spectrum is very sensitive to the intensity of the radiation field. For the molecular phase, which is probably associated with the Merope molecular cloud, we select a low value of  $\chi = 0.03$ ,

<sup>9</sup> <http://www.tapir.caltech.edu/~yacine/spdust/spdust.html>

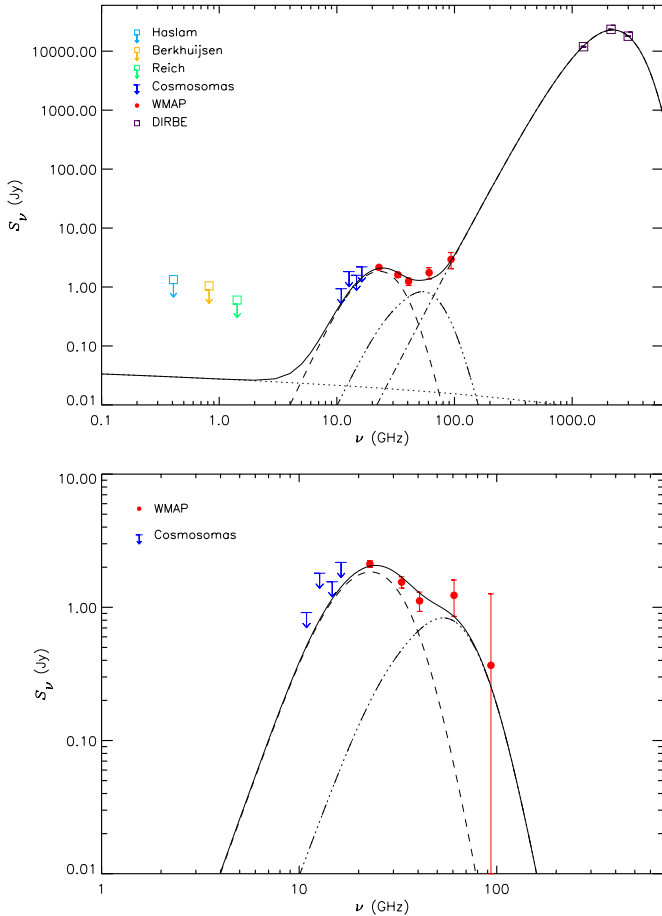


**Figure 8.** Top: same as in Figure 7, but for case B, i.e., a pixel-by-pixel subtraction of the CMB is performed, and then no CMB component is considered in the SED fitting. Fluxes for this case are quoted in Table 1. The fitted model consists of free–free emission (dotted line), thermal dust (dash-dotted line), and two spinning dust components: high-density molecular gas (dashed line) and low-density atomic gas (dash-triple-dotted line). The model parameters are listed in Table 2. Bottom: residual SED after subtraction of the free–free and best-fit thermal dust components.

(A color version of this figure is available in the online journal.)

in order to have the peak at  $\approx 23$  GHz, matching the *WMAP* *K*-band flux, which is our maximum measured value.

Ritchey et al. (2006) have calculated the intensity of the radiation field in different lines of sight toward the Pleiades; from their values (see their Table 6) in positions within our aperture we calculate an average of  $\chi \approx 16$ . Using this value and a hydrogen density of  $n_{\text{H}} = 30.6 \text{ cm}^{-3}$  (also calculated from an average of their measurements), and same values for the rest of the *SPDUST.2* input parameters, we obtain a spinning dust spectrum which peaks at 36.9 GHz and provides a very poor fit to the data. If we use for the hydrogen number density a value as low as  $n_{\text{H}} = 0.03 \text{ cm}^{-3}$ , while maintaining the same radiation field intensity, the spectrum peaks at a lower value of 31 GHz, still far from the observed peak around 22.8 GHz. Therefore, in order to reliably fit the data, we have to decrease the intensity of the radiation field for the molecular phase. Note however that Ritchey et al. (2006) do not provide measurements for the radiation field in any position toward the Merope molecular cloud, and therefore it could be the case that its intensity is indeed lower. On the other hand, for the atomic phase, which probably traces a more diffuse component scattered around the clouds, we adopt  $\chi = 10$ , which is closer to the values reported

**Table 2**  
Model Parameters

$T_e$ (K)	8000	
EM ( $\text{cm}^{-6}$ pc)	0.267	
	Molecular	Atomic
$n_{\text{H}}$ ( $\text{cm}^{-3}$ )	300	200
$T_{\text{g}}$ (K)	20	1000
$\chi$	0.03	10
$x_{\text{H}}$ (ppm)	9.2	373
$x_{\text{C}}$ (ppm)	1	100
$y$	1	0.1
$\beta$ (D)	9.34	9.34
	Case A	
$N_{\text{H}}$ ( $10^{20} \text{ cm}^{-2}$ )	$6.94 \pm 0.22$	...
$\tau_{100}$	$(6.09 \pm 0.06) \times 10^{-4}$	
$\beta_{\text{d}}$	$2.29 \pm 0.02$	
$T_{\text{d}}$ (K)	$20.12 \pm 0.03$	
$\Delta T_{\text{cmb}}$ ( $\mu\text{K}$ )	$42.2 \pm 1.9$	
	Case B	
$N_{\text{H}}$ ( $10^{20} \text{ cm}^{-2}$ )	$6.60 \pm 0.11$	$0.30 \pm 0.01$
$\tau_{100}$	$(3.302 \pm 0.004) \times 10^{-4}$	
$\beta_{\text{d}}$	$1.869 \pm 0.004$	
$T_{\text{d}}$ (K)	$22.008 \pm 0.005$	

**Notes.** The two values on the top of the table define the spectrum of the free–free emission.  $T_e$  is an assumed value, and EM is calculated from the  $\text{H}\alpha$  intensity corrected from Galactic extinction (see Section 3.1). Parameters from  $n_{\text{H}}$  to  $\beta$  (see Section 4 for an explanation of their meanings) are used as inputs for the spinning-dust models. They are fixed at typical values for the two different gas phases (molecular and atomic). The rest of the parameters are jointly fitted to the spectrum.  $N_{\text{H}}$  defines the amplitude of the spinning dust component;  $\tau_{100}$ ,  $\beta_{\text{d}}$ , and  $T_{\text{d}}$  define the thermal dust spectrum; and  $\Delta T_{\text{cmb}}$  is the average value of the CMB temperature within the aperture. This CMB component is fitted only in case A, as in case B we calculate the fluxes on CMB-subtracted maps. Also, in case A no atomic gas phase producing spinning-dust emission was considered.

by Ritchey et al. (2006), and also provides a better fit to the 60.8 GHz point. Once we have obtained the spinning dust spectra for the molecular and atomic phases from *SPDUST.2*, their amplitudes, which are defined by the hydrogen column densities  $N_{\text{H}}$ , are fitted to the measured fluxes.

We model the thermal dust, which is the main contribution at infrared frequencies, through a modified blackbody spectrum,  $I_{\nu}^{\text{d}}(T_{\text{d}}) = \tau_{100}(\nu/(2998 \text{ GHz}))^{\beta_{\text{d}}} B_{\nu}(T_{\text{d}})$ , with  $T_{\text{d}}$  being the dust temperature,  $\tau_{100}$  the optical depth at  $100 \mu\text{m}$ , and  $\beta_{\text{d}}$  the emissivity spectral index. The free–free spectrum is normalized by assuming an electron temperature  $T_e = 8000$  K and estimating the electron measure, indicated in Table 2, through the extinction-corrected  $\text{H}\alpha$  emission in the region (see Section 3.1). This spectrum is represented by the dotted lines of Figures 7 and 8.

In the SED of case A (Figure 7) the CMB is probably contaminating our measurements and boosting the *WMAP* *V*- and *W*-band fluxes. Therefore, in this case we also fit to the data a CMB component with an average temperature  $\Delta T_{\text{cmb}}$ , and neglect the spinning dust corresponding to the atomic gas phase, as it would be completely overshadowed by the CMB component. After subtracting the free–free flux corresponding to each frequency, we jointly fit, using a nonlinear least-squares method, our five model parameters,  $N_{\text{H}}$ ,  $\Delta T_{\text{cmb}}$ ,  $T_{\text{d}}$ ,  $\tau_{100}$ , and  $\beta_{\text{d}}$ , defining the spinning dust, CMB, and thermal dust components, to the *WMAP* and *DIRBE* fluxes. In case B (Figure 8), we fit the hydrogen column density associated with the spinning-dust

atomic phase instead of  $\Delta T_{\text{cmb}}$ , as the CMB has been removed directly from the map. The fitted parameters and their errors are shown in Table 2, and the spectra of all components are represented in Figures 7 and 8. We see that these fitted spectra are indeed fully compatible with the COSMOSOMAS  $3\sigma$  upper limits. The reduced chi-squares are 0.75 and 6.76 for cases A and B, respectively.

The dust temperature is somewhat higher in case B, with the spectrum being steeper in case A. This is a consequence of  $\Delta T_{\text{cmb}}$  in case B being slightly larger than the average ILC temperature within the aperture,  $30.2 \mu\text{K}$ , which is the effective CMB level that we are subtracting in case A prior to flux calculation. The fitted values for the hydrogen column densities are compatible in both cases. These values show that the Pleiades reflection nebula constitutes indeed a more diffuse medium than others where AME has been usually studied, such as the Perseus and  $\rho$  Ophiuchus molecular clouds, where  $N_{\text{H}} = 117 \times 10^{20} \text{ cm}^{-2}$  and  $171 \times 10^{20} \text{ cm}^{-2}$ , respectively (Planck Collaboration et al. 2011). This also becomes evident from the reddening measurements in this region,  $E_{B-V} = 0.1 \text{ mag}$  (see Section 3.1), which are typical of diffuse clouds, and lower than the respective values in the Perseus and  $\rho$  Ophiuchus molecular clouds, and even lower than the reddening of the translucent cloud LDN 1780,  $E_{B-V} \sim 0.6$ , where Vidal et al. (2011) have recently found AME. Our fitted values for the hydrogen column densities are also of the same order of those derived by applying the scaling relation of Bohlin et al. (1978),  $(N_{\text{H}} + N_{\text{H}_2})/E_{B-V} = 5.8 \times 10^{21} \text{ cm}^{-2} \text{ mag}^{-1}$ , and taking for the reddening  $E_{B-V} = 0.1 \text{ mag}$ . It may also be noted that by dividing the fitted hydrogen column density of the molecular phase by the hydrogen number density, we get an estimate for the depth of the cloud of  $\sim 0.7 \text{ pc}$ , a value that agrees with the characteristic length scale of this cloud.

It is also interesting to compare our results with those presented in Figure 13 of Vidal et al. (2011), where they plot emissivity at 31 GHz (intensity at 31 GHz divided by hydrogen column density) versus hydrogen column density. Dividing the total flux at 33 GHz for case B by the solid angle of the aperture and by the corresponding fitted column density we get  $\epsilon_{33} = (2.55 \pm 0.28) \times 10^{-24} \text{ MJy sr}^{-1} \text{ cm}^2$ . In order to scale to 31 GHz we use our fitted model and obtain  $\epsilon_{31} = (3.03 \pm 0.33) \times 10^{-24} \text{ MJy sr}^{-1} \text{ cm}^2$ . This value roughly follows the trend shown in that figure, but falls below the fitted line, which for  $N_{\text{H}} = 6.60 \times 10^{20} \text{ cm}^{-2}$  predicts  $\sim 5.7 \times 10^{-24} \text{ MJy sr}^{-1} \text{ cm}^2$ . It therefore seems that the Pleiades nebula, in addition to having a notable lower hydrogen column density to the regions shown in that figure, and actually to the majority of the regions where AME had been previously detected, also has a lower emissivity per hydrogen nucleon.

The residual fluxes, obtained after subtracting all modeled components except the spinning dust, are quoted in Table 1 and plotted in the bottom panels of Figures 7 and 8. According to our fitted model for case B, the thermal dust contributes at 22.8 GHz with a flux of 0.012 Jy, whereas the level of the free-free at this frequency was 0.019 Jy. Then, the residual flux at this frequency, which can be attributed to AME, is  $2.12 \pm 0.12 \text{ Jy}$  ( $17.7\sigma$ ; modeling errors included).

## 5. CONCLUSIONS

We have presented evidence for AME in the position of the nearby (125 pc) Pleiades star cluster, one of the most studied regions in the sky. This AME originates in the dust grains that make up the Pleiades reflection nebula, whose thermal infrared emission was discovered by Castelaz et al. (1987). Using data

from the seven-year release of *WMAP*, here we have measured a total flux density toward this nebulosity of  $2.15 \pm 0.12 \text{ Jy}$  at 22.8 GHz by applying an aperture integration in a  $1^\circ$  radius circle around the position (R.A., decl.) =  $56^\circ 24' + 23^\circ 78'$  (J2000). COSMOSOMAS maps at 11–17 GHz do not show evidence for emission at this position. Nevertheless, we have set upper limits (99.7% C.L.) of 0.94 Jy at 10.9 GHz and 1.58 Jy at 13.6 GHz, which help to trace the downturn of the AME spectrum at these frequencies predicted by models based on electric dipole emission from fast-spinning dust grains.

In order to quantify the total AME flux we have considered other emission mechanisms. We have estimated a free-free flux of 0.019 Jy, at the same reference frequency of 22.8 GHz, from the  $\text{H}\alpha$  map of Schlegel et al. (1998), which had been previously corrected from Galactic extinction by using reddening values measured toward different stars. Infrared fluxes obtained from the *COBE*-DIRBE experiment have been used to trace the thermal dust emission, from which we extrapolate to microwave frequencies and obtain a flux of 0.012 Jy. Therefore, both the free-free and thermal dust emissions have little impact in our measurement. After deducting these two components we have obtained a residual flux of  $2.12 \pm 0.12 \text{ Jy}$ , which is a detection of AME at the  $17.7\sigma$  level.

The signal at 22.8 GHz is slightly resolved by the *WMAP* *K*-band beam ( $0^\circ:85$  FWHM). This indicates that, although the bulk of the emission is probably from the region near the stars 23 Tau and 17 Tau, where the strongest infrared emission is also detected, there is probably an important diffuse component integrated over the whole nebulosity. Observations with microwave experiments at higher angular resolution are crucial to elucidate the relative contribution to the total observed flux of the different individual clouds that constitute the Pleiades reflection nebula. They may also help to better trace the correlation with the thermal dust and to shed light on the properties of the grain population that may be originating this AME.

After deducting the extrapolated free-free fluxes, we have fitted a joint model consisting of a modified blackbody spectrum, tracing the thermal dust emission, and a spinning-dust spectrum which traces the AME, to the *WMAP* and DIRBE fluxes. For the spinning-dust component we have considered two complementary phases, one dominated by high-density molecular gas and the other by lower density atomic gas. Their spinning-dust spectra have been obtained with *SPDUST.2* by using realistic values for the physical parameters that are inputs to this code. We then fitted the amplitude of the spectra to the data, together with the three parameters that define the thermal dust model. The resulting spinning-dust fit successfully traces the *WMAP* and DIRBE data, while being compatible with the COSMOSOMAS upper limits.

Microwave temperatures at 22.8 GHz are clearly correlated with  $100 \mu\text{m}$  infrared intensities, the dust emissivity being  $4.36 \pm 0.17 \mu\text{K} (\text{MJy sr}^{-1})^{-1}$ . This value is lower than what is typical in cool dust clouds, and more characteristic of H II regions. The physical properties of the Pleiades nebula show that this is a much less opaque medium than others where AME has been generally studied, the reason for this detection likely being its proximity. For instance, the optical depth and the hydrogen column density of the Perseus molecular cloud are more than an order of magnitude higher (Watson et al. 2005; Planck Collaboration et al. 2011), which explains why the AME flux at 22.8 GHz is there 20 times larger than in the Pleiades despite being at twice their distance. This potentially makes the

Pleiades an attractive environment to study the AME emission in different physical conditions than those generally explored up to now.

We thank the referee for useful comments, which helped to extend the discussion on some important aspects. The color-scale image of Figure 1 is based on photographic data obtained using the Oschin Schmidt Telescope on Palomar Mountain. The Palomar Observatory Sky Survey was funded by the National Geographic Society. The Oschin Schmidt Telescope is operated by the California Institute of Technology and Palomar Observatory. The plates were processed into the present compressed digital format with their permission. The Digitized Sky Survey was produced at the Space Telescope Science Institute (STScI) under U.S. Government grant NAG W-2166. We acknowledge the use of the MPIFR Survey Sampler Web site at <http://www.mpifr-bonn.mpg.de/survey.html>, from which we obtained the 0.820 GHz data. We acknowledge the use of the Legacy Archive for Microwave Background Data Analysis (LAMBDA). Support for LAMBDA is provided by the NASA Office of Space Science. Some of the results in this paper have been obtained using the HEALPix (Górski et al. 2005) package. This work has been partially funded by project AYA2010-21766-C03-02 of the Spanish Ministry of Science and Innovation (MICINN). J.A.R.-M. is a Ramón y Cajal fellow of the MICINN.

## REFERENCES

- Ali-Haïmoud, Y., Hirata, C. M., & Dickinson, C. 2009, *MNRAS*, **395**, 1055
- Ami Consortium: Scaife, A. M. M., Hurley-Walker, N., Green, D. A., et al. 2009a, *MNRAS*, **394**, L46
- Ami Consortium: Scaife, A. M. M., Hurley-Walker, N., Green, D. A., et al. 2009b, *MNRAS*, **400**, 1394
- Battistelli, E. S., Rebolo, R., Rubiño-Martín, J. A., et al. 2006, *ApJ*, **645**, L141
- Bennett, C. L., Hill, R. S., Hinshaw, G., et al. 2003, *ApJS*, **148**, 97
- Bennett, C. L., Hinshaw, G., Banday, A., et al. 1993, *ApJ*, **414**, L77
- Berkhuijsen, E. M. 1972, *A&AS*, **5**, 263
- Bohlin, R. C., Savage, B. D., & Drake, J. F. 1978, *ApJ*, **224**, 132
- Casassus, S., Cabrera, G. F., Förster, et al. 2006, *ApJ*, **639**, 951
- Casassus, S., Dickinson, C., Cleary, K., et al. 2008, *MNRAS*, **391**, 1075
- Castelaz, M. W., Sellgren, K., & Werner, M. W. 1987, *ApJ*, **313**, 853
- Castellanos, P., Casassus, S., Dickinson, S., et al. 2011, *MNRAS*, **411**, 1137
- Cernis, K. 1987, *Ap&SS*, **133**, 355
- Condon, J. J., Cotton, W. D., Greisen, E. W., et al. 1998, *AJ*, **115**, 1693
- Dame, T. M., Hartmann, D., & Thaddeus, P. 2001, *ApJ*, **547**, 792
- Davies, R. D., Dickinson, C., Banday, A. J., et al. 2006, *MNRAS*, **370**, 1125
- de Oliveira-Costa, A., Kogut, A., Devlin, M. J., et al. 1997, *ApJ*, **482**, L17
- de Oliveira-Costa, A., Tegmark, M., Davies, R. D., et al. 2004, *ApJ*, **606**, L89
- de Oliveira-Costa, A., Tegmark, M., Gutierrez, C. M., et al. 1999, *ApJ*, **527**, L9
- de Oliveira-Costa, A., Tegmark, M., Page, L. A., & Boughn, S. P. 1998, *ApJ*, **509**, L9
- Dickinson, C., Davies, R. D., Allison, J. R., et al. 2009, *ApJ*, **690**, 1585
- Dickinson, C., Davies, R. D., Bronfman, L., et al. 2007, *MNRAS*, **379**, 297
- Dickinson, C., Davies, R. D., & Davis, R. J. 2003, *MNRAS*, **341**, 369
- Draine, B. T., & Lazarian, A. 1998a, *ApJ*, **494**, L19
- Draine, B. T., & Lazarian, A. 1998b, *ApJ*, **508**, 157
- Draine, B. T., & Lazarian, A. 1999, *ApJ*, **512**, 740
- Erickson, W. C. 1957, *ApJ*, **126**, 480
- Federman, S. R., & Willson, R. F. 1984, *ApJ*, **283**, 626
- Fernández-Cerezo, S., Gutiérrez, C. M., Rebolo, R., et al. 2006, *MNRAS*, **370**, 15
- Finkbeiner, D. P. 2003, *ApJS*, **146**, 407
- Finkbeiner, D. P. 2004, *ApJ*, **614**, 186
- Finkbeiner, D. P., Schlegel, D. J., Frank, C., & Heiles, C. 2002, *ApJ*, **566**, 898
- Gallegos, J. E., Macías-Pérez, J. F., Gutiérrez, C. M., et al. 2001, *MNRAS*, **327**, 1178
- Gibson, S. J., & Nordsieck, K. H. 2003, *ApJ*, **589**, 362
- Gold, B., Odegard, N., Weiland, J. L., et al. 2011, *ApJS*, **192**, 15
- Gordon, K. J., & Army, T. T. 1984, *AJ*, **89**, 672
- Górski, K. M., Hivon, E., Banday, A. J., et al. 2005, *ApJ*, **622**, 759
- Haslam, C. G. T., Salter, C. J., Stoffel, H., & Wilson, W. E. 1982, *A&AS*, **47**, 1
- Hauser, M. G., Arendt, R. G., Kelsall, T., et al. 1998, *ApJ*, **508**, 25
- Herbig, G. H., & Simon, T. 2001, *AJ*, **121**, 3138
- Hernández-Monteagudo, C., & Rubiño-Martín, J. A. 2004, *MNRAS*, **347**, 403
- Hildebrandt, S. R., Rebolo, R., Rubiño-Martín, J. A., et al. 2007, *MNRAS*, **382**, 594
- Hoang, T., Draine, B. T., & Lazarian, A. 2010, *ApJ*, **715**, 1462
- Hoang, T., Lazarian, A., & Draine, B. T. 2011, arXiv:1105.2302
- Iglesias-Groth, S. 2005, *ApJ*, **632**, L25
- Iglesias-Groth, S. 2006, *MNRAS*, **368**, 1925
- Jarosik, N., Bennett, C. L., Dunkley, J., et al. 2011, *ApJS*, **192**, 14
- Kogut, A., Banday, A. J., Bennett, C. L., et al. 1996a, *ApJ*, **460**, 1
- Kogut, A., Banday, A. J., Bennett, C. L., et al. 1996b, *ApJ*, **464**, L5
- Kogut, A., Dunkley, J., Bennett, C. L., et al. 2007, *ApJ*, **665**, 355
- Kogut, A., Fixsen, D. J., Levin, S. M., et al. 2011, *ApJ*, **734**, 4
- Lazarian, A., & Draine, B. T. 2000, *ApJ*, **536**, L15
- Leitch, E. M., Readhead, A. C. S., Pearson, T. J., & Myers, S. T. 1997, *ApJ*, **486**, L23
- López-Caraballo, C. H., Rubiño-Martín, J. A., Rebolo, R., & Génova-Santos, R. 2011, *ApJ*, **729**, 25
- Mason, B. S., Robishaw, T., Heiles, C., Finkbeiner, D., & Dickinson, C. 2009, *ApJ*, **697**, 1187
- Mather, J. C., Fixsen, D. J., Shafer, R. A., Mosier, C., & Wilkinson, D. T. 1999, *ApJ*, **512**, 511
- O'Donnell, J. E. 1994, *ApJ*, **422**, 158
- Planck Collaboration: Ade, P. A. R., Aghanim, N., Arnaud, M., et al. 2011, arXiv:1101.2031
- Platania, P., Burigana, C., Maino, D., et al. 2003, *A&A*, **410**, 847
- Reich, P., & Reich, W. 1986, *A&AS*, **63**, 205
- Ritchey, A. M., Martínez, M., Pan, K., Federman, S. R., & Lambert, D. L. 2006, *ApJ*, **649**, 788
- Schlegel, D. J., Finkbeiner, D. P., & Davis, M. 1998, *ApJ*, **500**, 525
- Silsbee, K., Ali-Haïmoud, Y., & Hirata, C. M. 2011, *MNRAS*, **411**, 2750
- Tempel, W. 1861, *Astron. Nachr.*, **54**, 285
- Tibbs, C. T., Watson, R. A., Dickinson, C., et al. 2010, *MNRAS*, **402**, 1969
- van Leeuwen, F. 1999, *A&A*, **341**, L71
- Vidal, M., Casassus, S., Dickinson, C., et al. 2011, *MNRAS*, **414**, 2424
- Watson, R. A., Rebolo, R., Rubiño-Martín, J. A., et al. 2005, *ApJ*, **624**, L89
- Weingartner, J. C., & Draine, B. T. 2001, *ApJ*, **548**, 296
- White, R. E. 1984, *ApJ*, **284**, 685
- White, R. E. 2003, *ApJS*, **148**, 487
- White, R. E., Allen, C. L., Forrester, W. B., Gonnella, A. M., & Young, K. L. 2001, *ApJS*, **132**, 253